Supporting information

Two-Dimensional Defective Boron-Doped Niobic Acid Nanosheets for Robust Nitrogen Photofixation

Yanting Zhang,[‖†] Lei Ran,[‖‡] Yanxue Zhang,[‖†] Panlong Zhai,[‖†] Yunzhen Wu,[†] Junfeng Gao,[‡] Zhuwei Li,[†] Bo Zhang,[†] Chen Wang,[†] Zhaozhong Fan,[†] Xiaomeng Zhang,[†] Jiaqi Cao,[†] Dingfeng Jin,[†] Licheng Sun,[¶⊥] and Jungang Hou[*†]

[†]State Key Laboratory of Fine Chemicals, School of Chemical Engineering, Dalian University of Technology, Dalian 116024, P. R. China.

[‡]Laboratory of Materials Modification by Laser, Ion and Electron Beams (Dalian University of Technology), Ministry of Education, Dalian 116024, P. R. China.

[¶]Center of Artificial Photosynthesis for Solar Fuels, School of Science, Westlake University, Hangzhou 310024, P. R. China.

[⊥]Department of Chemistry, School of Engineering Sciences in Chemistry, Biotechnology and Health, KTH Royal Institute of Technology, 10044 Stockholm, Sweden.

These authors contributed equally: Yanting Zhang, Lei Ran, Yanxue Zhang and Panlong Zhai.

Supplementary experimental details.

Chemicals.

Niobium chloride ($NbCl_5$, 99%), tetramethylammonium hydroxide solution (TMAOH, 25%), sodium borohydride ($NaBH_4$, 98.0%), sodium hydroxide (NaOH, 99.9%), salicylic acid ($C_7H_6O_3$, 99.5%), sodium citrate ($C_6H_5Na_3O_7$, 98%), sodium hypochlorite solution (NaClO, 6~14%), sodium nitroferricyanide dihydrate ($C_5FeN_6Na_2O{\cdot}2H_2O$, 99%), para-(dimethylamino) benzaldehyde ($C_9H_{11}NO$), hydrazine hydrate ($N_2H_4{\cdot}H_2O$, 85%), ammonia chloride (NH_4Cl), ammonium sulfate ($(NH_4)_2SO_4$, 10% ^{15}N and 90% ^{14}N) were purchased from Aladdin Chemistry Co., Ltd. All the materials were of analytical grade and used without further purification. Dimethyl sulfoxide-d_6 (DMSO-d_6) was purchased from Sigma-Aldrich. The $^{15}N_2$ was purchased from Wuhan Newradar Special Gas Co., Ltd. All chemicals were used without any purification and hydrochloric acid (HCl, 12 mol L^{-1}), absolute ethanol, acetone and deionized water with a resistivity of 18.25 MΩ cm^{-1}, were used throughout the experiments.

Synthesis of 2D HNb_3O_8 nanosheets.

The HNb_3O_8 nanosheets were prepared by the hydrothermal synthesis method. Typically, 12 mmol of $NbCl_5$ was dissolved in 40 mL of absolute ethanol with stirring in a 100 mL flask. Then, 40 mL of TMAOH solution was added dropwise into the above solution under drastically stirring. The mixture solution was transferred into 100 mL Teflon-lined stainless-steel autoclave followed by heated in an oven at 200~240 ℃ for 12 h. Then the autoclave was cooled to room temperature naturally. The product was washed with acetone, water and ethanol for three times to remove any possible remnants, respectively. Finally, the attained product was dried at 60 ℃ overnight under vacuum.

Synthesis of 2D B-V_o-$HNbO_3$ NSs.

TMA^+-Nb precursors were prepared by hydrothermal process.[1] 0.2 g TMA^+-Nb precursors were placed in 6 M HNO_3 solution and sonicated for 30 min. Then, the suspension was stirred for 1 day to ion exchange TMA^+ to H^+, leading to the formation of ultrathin HNb_3O_8 nanosheets (2D HNb_3O_8 NSs). After the mixture of 0.4 g HNb_3O_8 NSs and a certain amount of $NaBH_4$, boron-doped and oxygen-vacancies-confined $HNbO_3$ (B-V_o-$HNbO_3$) was

obtained by thermal treatment at different temperatures from 300~600 ℃ in argon atmosphere. Finally, the dispersed B-V_o-$HNbO_3$ NSs were produced through the subsequent extraction of the suspension by the ultrasonication approach.

Synthesis of 2D B-HNb_3O_8 NSs. TMA^+-Nb precursors were prepared by hydrothermal process.[1] 0.2 g TMA^+-Nb precursors were placed in 6 M HNO_3 solution and sonicated for 30 min. Then, the suspension was stirred for 1 day to ion exchange TMA^+ to H^+, leading to the formation of ultrathin HNb_3O_8 nanosheets (2D HNb_3O_8 NSs). After the mixture of HNb_3O_8 NSs and a certain amount of H_3BO_3, boron-doped HNb_3O_8 (B-HNb_3O_8) was obtained by thermal treatment at 300~600 ℃ in argon atmosphere. Finally, the dispersed B-HNb_3O_8 NSs were produced through the subsequent extraction of the suspension by the ultrasonication approach.

Synthesis of 2D V_o-HNb_3O_8 NSs. TMA^+-Nb precursors were prepared by hydrothermal process.[1] 0.2 g TMA^+-Nb precursors were placed in 6 M HNO_3 solution and sonicated for 30 min. Then, the suspension was stirred for 1 day to ion exchange TMA^+ to H^+, leading to the formation of ultrathin HNb_3O_8 nanosheets (HNb_3O_8 NSs). Oxygen-vacancies-confined HNb_3O_8 (V_o-HNb_3O_8) was obtained by the room-temperature reduction in a $NaBH_4$ solution with ethanol as the solvent. Finally, the dispersed V_o-HNb_3O_8 NSs were produced through the subsequent extraction of the suspension by the ultrasonication approach.

Synthesis of $HNbO_3$ powders. $HNbO_3$ powders were prepared by a molten-salt way and subsequent H^+–Li^+ ion-exchange reaction process.[2] Stoichiometric amounts of Nb_2O_5 and Li_2CO_3 were ground well to obtain uniform mixtures and mixed adequately with Li_2SO_4–Na_2SO_4 (1:1 molar ratio) in a Nb_2O_5–Li_2CO_3/Li_2SO_4–Na_2SO_4 mass ratio of 1 : 2. These mixtures were then heated to 700 °C for 1 h in alumina crucibles. After calcination, the salts were ultrasonically washed with hot distilled water for several times and then dried in air. As-obtained $LiNbO_3$ powders were dispersed into hot aqueous HNO_3 at 90~100 °C and stirred constantly for 72 h. The resulting $HNbO_3$ powders were washed and dried.

Synthesis of B-$HNbO_3$ powders. $HNbO_3$ powders as the precursors were used by a

molten-salt way and subsequent H^+–Li^+ ion-exchange reaction process. After the mixture of HNb_3O_8 powders and a certain amount of H_3BO_3, boron-doped $HNbO_3$ (B-$HNbO_3$) powders were obtained by thermal treatment at 300~600 ℃ in argon atmosphere and the subsequent ultrasonication treatment.

Synthesis of V_o-$HNbO_3$ powders. $HNbO_3$ powders as the precursors were used by a molten-salt way and subsequent H^+–Li^+ ion-exchange reaction process. Oxygen-vacancies-confined $HNbO_3$ (V_o-$HNbO_3$) powders were obtained by was obtained by the room-temperature reduction in a $NaBH_4$ solution with ethanol as the solvent and the subsequent ultrasonication treatment.

Synthesis of B-V_o-$HNbO_3$ powders. $HNbO_3$ powders as the precursors were used by a molten-salt way and subsequent H^+–Li^+ ion-exchange reaction process. After the mixture of $HNbO_3$ NSs and a certain amount of $NaBH_4$, boron-doped and oxygen-vacancies-confined $HNbO_3$ (B-V_o-$HNbO_3$) powders were obtained by thermal treatment at 300~600 ℃ in argon atmosphere.

Characterization.

Powder X-ray diffraction (XRD) patterns were tested by X-ray diffractometer equipped with graphite monochromatized Cu K_α radiation (λ = 1.54178 Å). SEM images were captured by a field-emission scanning electron microscope (SEM, FEI Nova Nano SEM 450). TEM images were performed on transmission electron microscopy (TEM, FEI TF30). Atomic force microscope (AFM) was performed by DI Innova Multimode SPM platform. N_2 adsorption-desorption curves were obtained by Micromeritics ASAP 2460 surface areas and porosities profiler. Specific surface area was acquired by Brunauer-Emmett-Teller (BET) approach. X-ray photoelectron spectroscopy (XPS, ESCALAB 250) pattern was applied to explore the elements composition and valence states of materials. UV-vis absorption and photoluminescence (PL) spectra were measured by UV-Vis-NIR spectrophotometer (Shimadzu UV-3600 Plus) and fluorescence spectrometer (Horiba, FloroMax-4P). Electron paramagnetic resonance (EPR) tests were performed under ambient room temperature through Bruker 500 spectrometer (Bruker E500).

Photocatalytic tests.

The photocatalytic performance of B-V_o-$HNbO_3$ NSs was evaluated for photocatalytic N_2 reduction at room temperature. Before the reaction, the photocatalysts were dispersed into pure water and pre-treated for 1 h by ultrasonic treatment. In a typical experiment, the N_2 fixation reaction was performed in a quartz reactor with a peristaltic pump. A 300 W Xenon lamp was employed as the optical light source. The catalyst (10 mg) was dispersed in pure water (20 mL) with sonication treatment for 10 min, bubbling with N_2 flow (30 mL min^{-1}) for 30 min. The reactor was then illuminated and then bubbled high-purity N_2 by the peristaltic pump with continuous stirring. An aliquot of the reaction solution (3.0 mL) was taken out every 1 h, then filtered and centrifuged to remove the residual photocatalyst. The concentration of NH_3 in supernatant was detected by colorimetry (Indophenol blue method) and ion chromatography (IonPac CS16, Dionex). The content of hydrazine (N_2H_4) species was monitored using para-(dimethylamino) benzaldehyde. The amount of oxygen was analyzed by the thermal conductivity detector (TCD) gas chromatograph.

Photoelectrochemical and electrochemical measurements.

The PEC measurements were performed on a CHI 760E electrochemical workstation equipped with the three-electrode cell. Firstly, the original FTO glasses were cleaned with acetone, ethanol and ultra-pure water. The working electrode was coated glass FTO electrode coated with the catalyst, dipcoating the electrode in a slurry consisting of 5 mg photocatalyst, 75 μL of 5 wt% nafion solution and 1 mL of absolute ethanol. The counter electrode was a platinum foil, the reference electrode was a saturated Ag/AgCl electrode, and the electrolyte was 0.5 M Na_2SO_4. The light source was a 300W Xe lamp with the light intensity was 100 mW cm^{-2}. The I-t curves were measured under chopped illumination at 1.23 V *vs*. RHE. The electrochemical impedance spectroscopy (EIS) measurements were conducted over a frequency range 0.1-10^5 Hz.

Quantification of ammonia by the indophenol blue method.

The ammonia concentration was spectrophotometrically determined by the indophenol blue method with modification.[3] In brief, 2 mL of 1 M NaOH solution containing salicylic acid (5 wt%) and sodium citrate (5 wt%) was added into 1 mL of the supernatant after N_2

photocatalytic reduction, followed by addition of 1 mL of 0.05 M NaClO and 200 μL of $C_5FeN_6Na_2O$ (1 wt%) for 1 h. The absorption spectrum was measured using an UV-vis spectrophotometer. The concentration of indophenol blue was determined using the absorbance at a wavelength of 655 nm. The concentration-absorbance curve was calibrated using standard ammonia chloride solutions with a serious of concentrations. According to the absorbance and standard curve, the concentration of the generated ammonia was obtained.

Quantification of ammonia by the ion chromatograph method.

To confirm the concentration of NH_4^+ precisely, we used the ion chromatograph method (IC).[4] During detection of NH_4^+, 30 mM of methane sulfonic acid was used as the eluent solution with a flow rate of 1 mL min^{-1}. The column temperature and self-regenerating suppressor (SRS) current were kept as 40 ℃ and 89 mA, respectively. 0.5 mL the supernatant was injected through the 25 μL quantitative injection loop to achieve standard analyte peaks for low concentrations of NH_4^+ cations, the retention time of NH_4^+ cations was about 8.7 min. The concentration curve was calibrated using standard ammonia chloride solutions with a serious of concentrations. According to the peak areas and standard curve, the concentration of the generated ammonia was obtained.

Determination of hydrazine.

The hydrazine concentration of the supernatant was estimated by the Watt and Chrisp method.[5] A mixture of para-(dimethylamino) benzaldehyde (5.99 g), HCl and absolute ethanol was used as a colour reagent. 2 mL of colour reagent was added to the supernatant, and the absorption spectrum was measured using a UV-vis spectrophotometer after 30 min at room temperature. The formation of hydrazine was determined by the absorbance at a wavelength of 455 nm. The concentration-absorbance curves were calibrated using standard hydrazine solutions with a serious of concentrations. According to the absorbance and standard curve, the concentration of the hydrazine was obtained.

$^{15}N_2$ isotope labelling experiment.

To confirm that the ammonia and hydrazine detected in the photocatalytic experiments

originated from dissolved N_2, further experiments were performed using $^{15}N_2$.[6] The $^{15}N_2$ was purchased from Wuhan Newradar Special Gas Co., Ltd. Before the photocatalytic reduction experiment, the reaction tube was charged and discharged with high-purity Ar, followed by pumping it to vacuum. Then the $^{15}N_2$ was purged into the system to reach atmospheric pressure. After $^{15}N_2$ photocatalytic reduction for 5 h under the 300 W Xe lamp, the supernatant was concentrated and the obtained $^{15}NH_4^+$ product was identified using ^1H NMR spectroscopy (Bruker AVANCE NEO 600M).

The detection of oxygen gas.

Oxygen gas (O_2) was detected by gas chromatography (GC) equipped with TCD detector using Ar and N_2 as the carrier gas. When the reaction was finished, detecting the amount of O_2 by gas chromatograph.

In-situ infrared spectroscopy tests.

The infrared tests were obtained using *in-situ* infrared cell.[7] *In-situ* infrared spectra were recorded by Nicolet IS50FT-IR spectrometer (Thermo, USA) with a designed reaction cell. The substrate lying in the center of the designed reaction cell was pre-deposited with a thin layer of B-V_o-$HNbO_3$ nanosheets. Then an ultra-high vacuum pump was used to pump out all the gases in the reaction cell and adsorbed on the photocatalyst surface. A layer of water molecules which were necessary to provide protons in our functional model was pre-adsorbed on the surface through bubbling a small amount of water vapor before the large amount of molecular nitrogen was pumped in to construct a N_2 atmosphere. At last, visible light was turned on and the IR signal was *in-situ* collected through a MCT detector along with the reaction.

Determination of apparent quantum efficiency and solar-to-ammonia efficiency.

The experiments for determining apparent quantum efficiency (AQE) and solar-to-ammonia (STA) efficiency were performed in pure water without sacrificial reagent. To obtain the AQE, the light was filtered by different monochromatic filters. The AQE was calculated by Equation.

$$AQE = \frac{N_e}{N_p} = \frac{6 \times N_{AM}}{N_p} = \frac{6 \times n_{AM} \times N_A}{\frac{W \times A \times t}{h \times v}} \times 100\% \qquad \text{(Equation. S1)}$$

where N_e, N_p, and N_{AM} represent the number of reacted electrons, incident photons, and generated ammonia, respectively; n_{AM} represents the molar number of generated ammonia; v, W, A, and t are the incident light frequency, intensity, irradiation area, and time, respectively; N_A and h are the Avogadro's constant and Planck constant, respectively.

The simulated AM1.5G sunlight was employed as the light source for measuring STA efficiency. The STA efficiency was determined by Equation.

$$STA = \frac{\Delta G_A \times n_A}{W \times A \times t} \times 100\% \quad \text{(Equation. S2)}$$

where ΔG_{AM} is the Gibbs free energy for ammonia generation from water and N_2 (339 kJ mol^{-1}); n_{AM} is the molar number of generated ammonia; W, A, and t represent the incident light intensity, irradiation area and time, respectively.

Calculation of band gap.

The band gap was estimated by following Tauc's relation:[8]

$$(\alpha h\nu)^2 = \alpha_0(h\nu - E_g) \quad \text{(Equation. S3)}$$

where h is Plank constant, v is frequency of incident light, α is absorption, E_g is optical band-gap and n is a constant. The electrode potential (*vs*. Ag/AgCl) was converted to RHE potential (E_{RHE}) according to Nernst Equation:[9]

$$E_{RHE} = E_{Ag/AgCl} + 0.059\,pH + E^o_{Ag/AgCl} \quad \text{(Equation. S4)}$$

$$E^o_{Ag/AgCl} = 0.1976\text{V}$$

where $E_{Ag/AgCl}$ was the applied potential *vs*. Ag/AgCl (which is the applied bias in this work), and another is the standard electrode potential of the Ag/AgCl at 25℃.

To acquire the band diagram of HNb_3O_8 from UPS spectra, the position of valance band (VB) maximum is obtained from the equation (S5~S6):

$$\varphi = h\nu - E_{cutoff} \quad \text{(Equation. S5)}$$

$$E_{VB} = E_F - X \quad \text{(Equation. S6)}$$

where φ is the work function; $h\nu$ = 21.2 eV; $E_{cuttoff}$ is the secondary electron onset obtained from the linear extrapolation of the UPS spectrum; E_F is the energy of the Fermi level, which is equivalent to the negative value for the work function ($-\varphi = E_F$); X is obtained from the extrapolation of the onsets in the UPS spectra.

The E_{VB} is *versus* vacuum level. According to the relationship between vacuum energy

level and the potential of the normal hydrogen electrode (NHE), the position of VB maximum *versus* NHE is described as the equation (S7):

$$E_{VB}^{*} = -E_{VB} - 4.5 \quad \text{(Equation. S7)}$$

Thus, the conduction band (CB) minimum potential (E_{CB}) can be easily calculated by the equation (S8):

$$E_{CB} = E_g - E_{VB} \quad \text{(Equation. S8)}$$

where E_g is the band gap from the Tauc plots by UV-Vis spectra.

Calculation of NH_3 production rate.

The ammonia production rate was calculated using the following equation:

$$C_{NH_3}(\mu mol\ g^{-1}h^{-1}) = N_{NH_4^+} / M_{Photocatalyst} \times T_{Illumination} \quad \text{(Equation. S9)}$$

where the N (NH_4^+) represents the mole numbers of generated ammonia, $M_{photocatalyst}$ is the quality of the photocatalyst used in reaction, $T_{Illumination}$ is the illumination time.

Density functional theory calculation.

The spin-polarized density functional theory (DFT) calculations implemented in the Vienna *ab Initio* Simulation Package (VASP) are employed to obtain the optimized structures, energetic and electronic properties of HNb_3O_8 and $HNbO_3$ slab models.[10] The electron exchange–correlation is described by generalized gradient approximation (GGA) with the functional of Perdew, Burke and Ernzerhof (PBE).[11] The Projector-augmented wave (PAW) was used to descript core electrons.[12] A plane-wave basis kinetic energy cutoff of 480 eV and a convergence criterion of 10^{-4} eV for the total energy and -0.03 eV/Å for the forces were used in our calculations. The Brillouin zone integration was performed using Monkhorst-Pack special k-points mesh of 2×4×1 for HNb_3O_8 slab model and 2×2×1 for $HNbO_3$ slab model. The van der Waals interaction is also considered by DFT-D3-BJ correction.[13]

The bulk HNb_3O_8 was optimized.[14,15] Then, the unit slab model of HNb_3O_8 was obtained by cutting the (010) surface of bulk HNb_3O_8. The unit slab model of $HNbO_3$ was obtained by cutting the (111) surface of primitive cell $HNbO_3$. The 2×2 supercell which contained four unit are adopted for HNb_3O_8 and $HNbO_3$ to simulated the NRR calculations. Especially, the bottom four layers of $HNbO_3$ are fixed during the structure optimized whereas the top two

layers are full relaxed. The B-V_o-$HNbO_3$ model was obtained by removed a surface O atom and substituted the nearby O atom with B atom. The vacuum space was set to 20 Å to avoid the interaction between two neighboring slabs.

The calculated adsorption energy was defined as:

$$E_{ads} = E_{Total} - E_{Sub} - E_A$$

where E_{Total} is the DFT total energy of the adsorption configuration, while E_{Sub} and E_A are energies of HNb_3O_8 or $HNbO_3$ slab substrate and the adsorbates, respectively.

The Gibbs free energy (G) of the intermediates of NRR was calculated by using the computational hydrogen electrode (CHE) model.[16] Based on this method, the G value was determined by the following equation.[17]

$$G = \Delta E - T\Delta S + \Delta ZPE$$

where ΔE, ΔZPE and ΔS are the differences in DFT total energy, zero-point energy and entropy between the adsorption species and the gas phase molecules. The temperature T is set as 298.15 K. The ΔZPE and ΔS of the NRR intermediate species were computed from their vibrational frequencies using the thermodynamic model within harmonic approximation. During these frequency calculations, all atoms of substrate were fixed whereas the adsorbates are fully relaxed. For gas-phase molecules, their zero-point energy and entropy values were taken from the NIST database.[18] The most positive ΔG (ΔG_{max}) of the entire NRR process is regarded as the rate-determining step (RDS). The onset potential of the whole reduction process is determined by ΔG_{max}, which can be deduced from $U_{onset} = -\Delta G_{max}/e$.

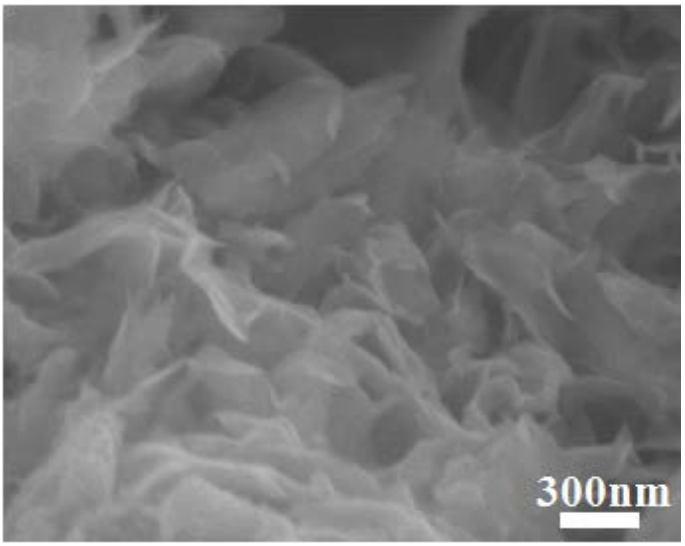

Figure S1. FESEM image of 2D HNb_3O_8 NSs.

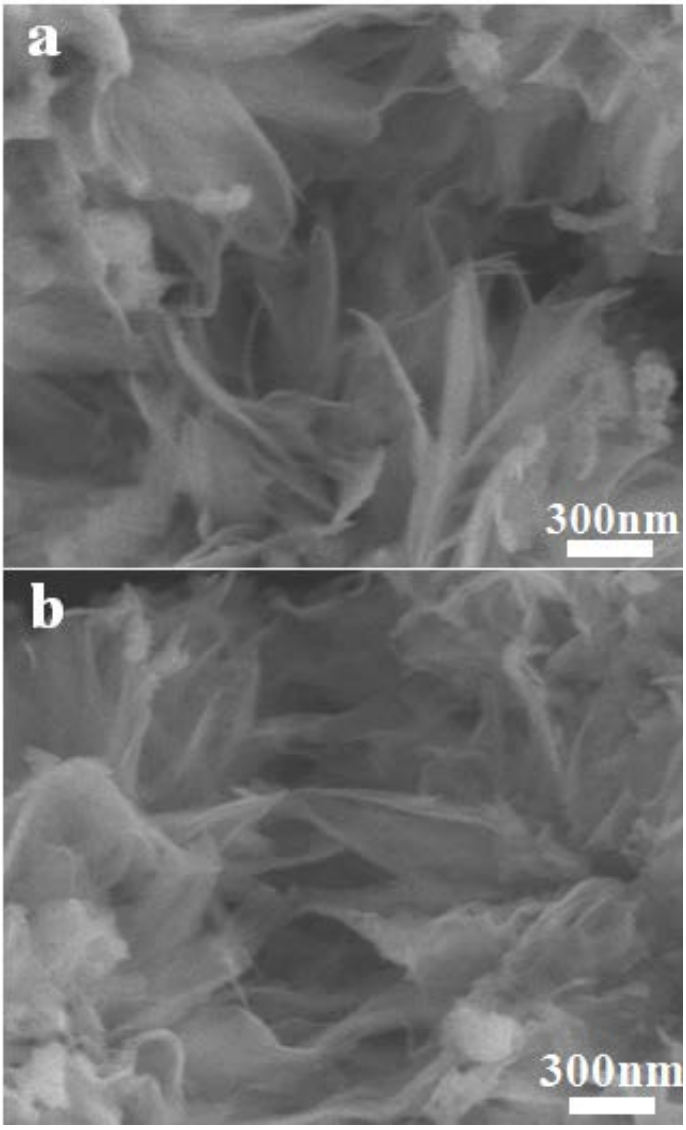

Figure S2. FESEM images of (a) V_o-HNb_3O_8 NSs and (b) B-V_o-$HNbO_3$ NSs.

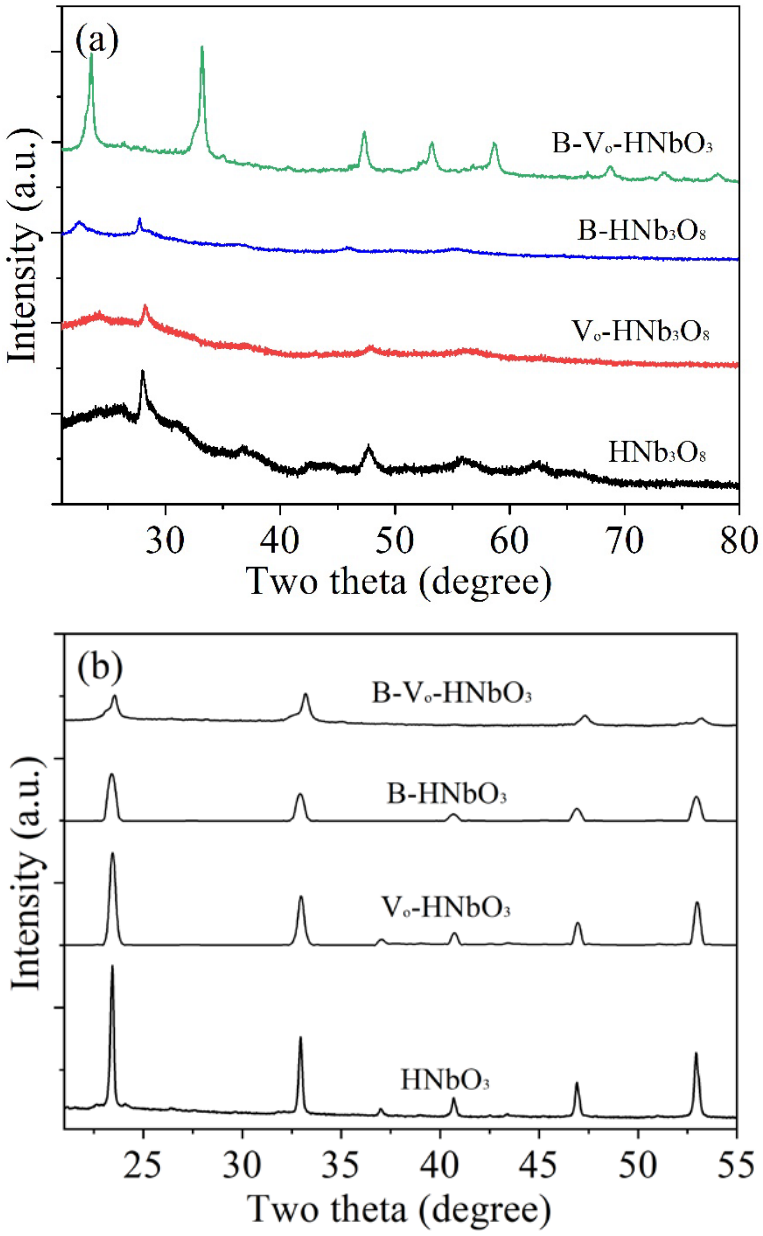

Figure S3. XRD patterns of (a) HNb_3O_8 nanosheets, V_o-HNb_3O_8 nanosheets, B-HNb_3O_8 nanosheets and B-V_o-$HNbO_3$ nanosheets by use of HNb_3O_8 nanosheets as the precursor, (b) $HNbO_3$ powders, V_o-$HNbO_3$ powders, B-$HNbO_3$ powders and B-V_o-$HNbO_3$ powders by use of $HNbO_3$ powders as the precursor.

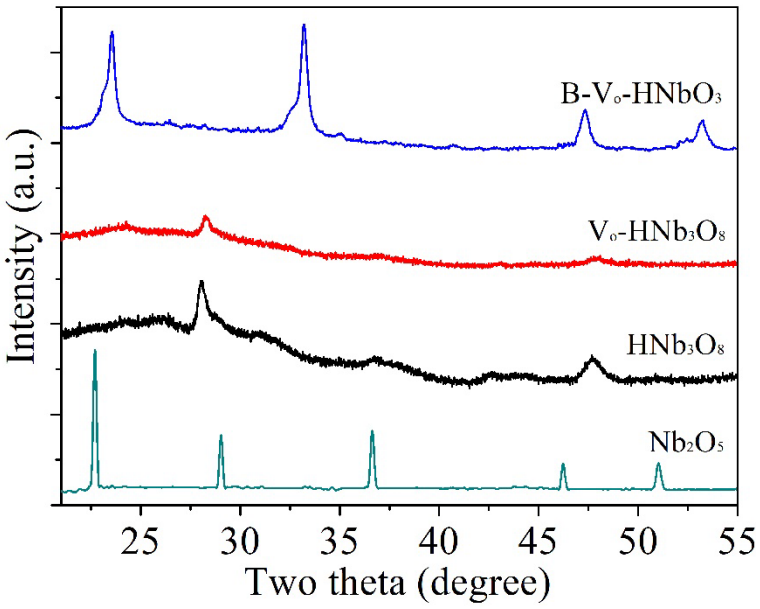

Figure S4. XRD pattern of commercial Nb_2O_5 powders.

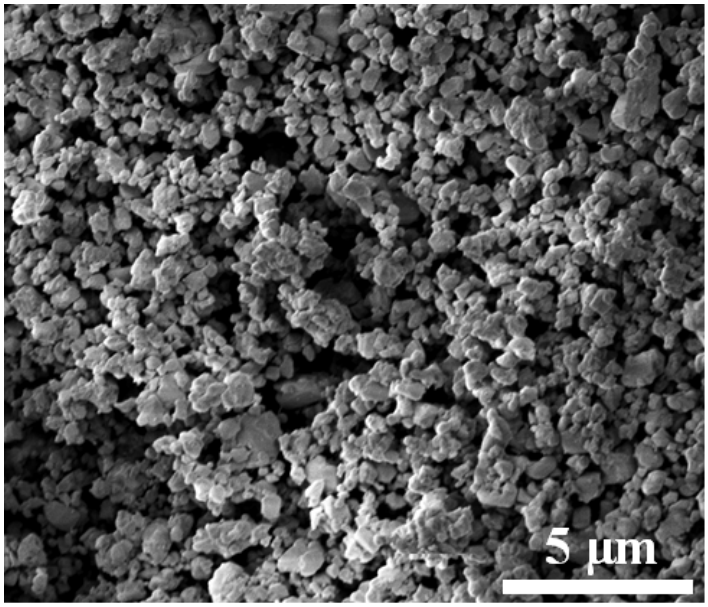

Figure S5. SEM image of B-V_o-$HNbO_3$ powders by use of $HNbO_3$ powders as the precursor.

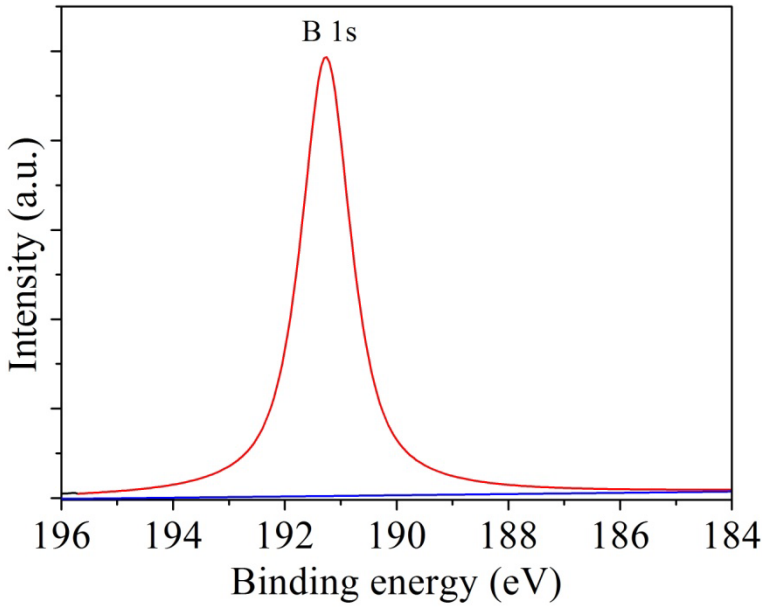

Figure S6. High-resolution B 1s XPS spectra of B-V_o-$HNbO_3$ NSs under the temperature at 500^{o}C.

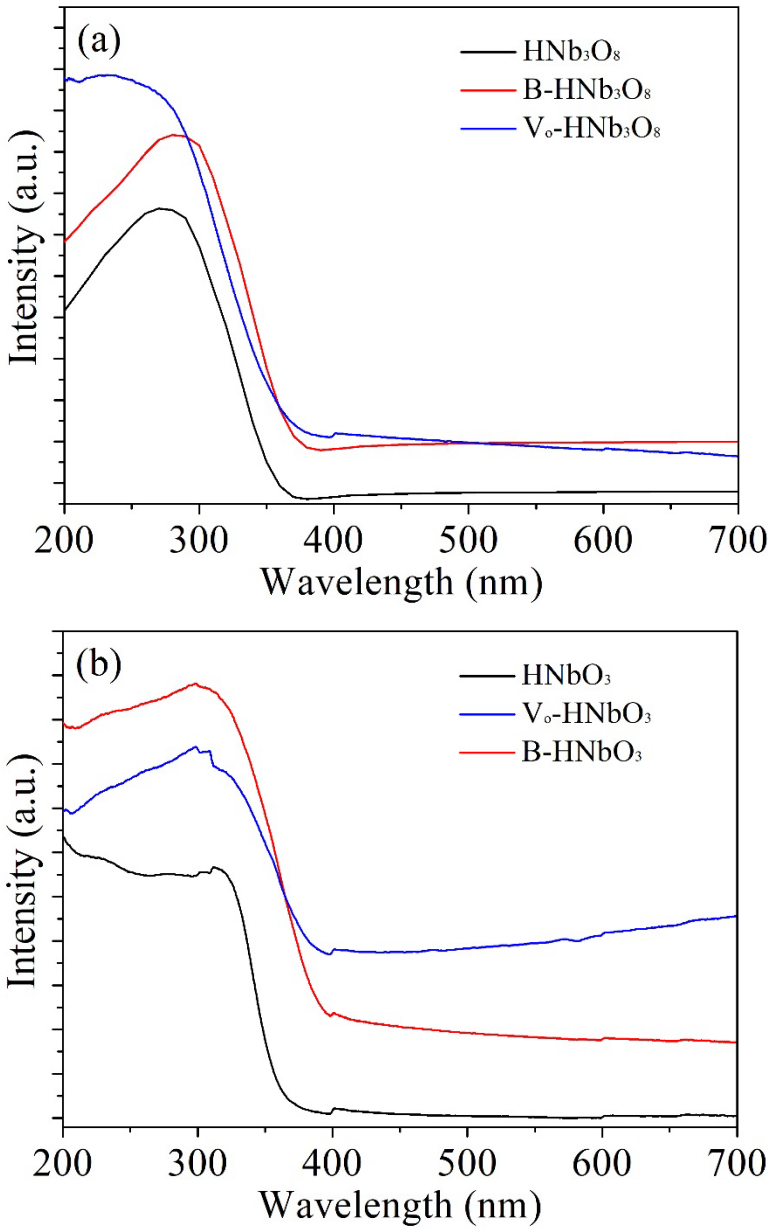

Figure S7. UV-vis absorption spectra of (a) HNb_3O_8, V_o-HNb_3O_8 and B-HNb_3O_8, (b) $HNbO_3$, V_o-$HNbO_3$ and B-$HNbO_3$ materials after thermal treatments by the introduction of boron dopant and oxygen vacancies.

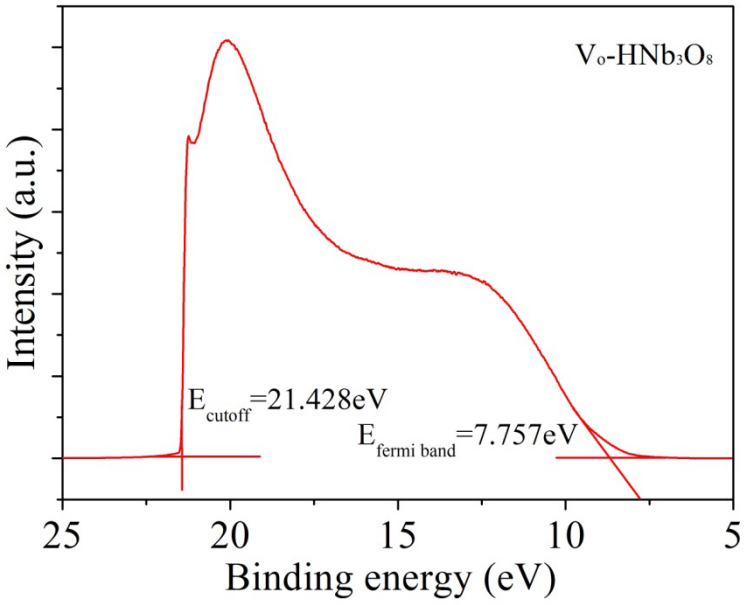

Figure S8. UPS spectra of V_o-HNb_3O_8 NSs.

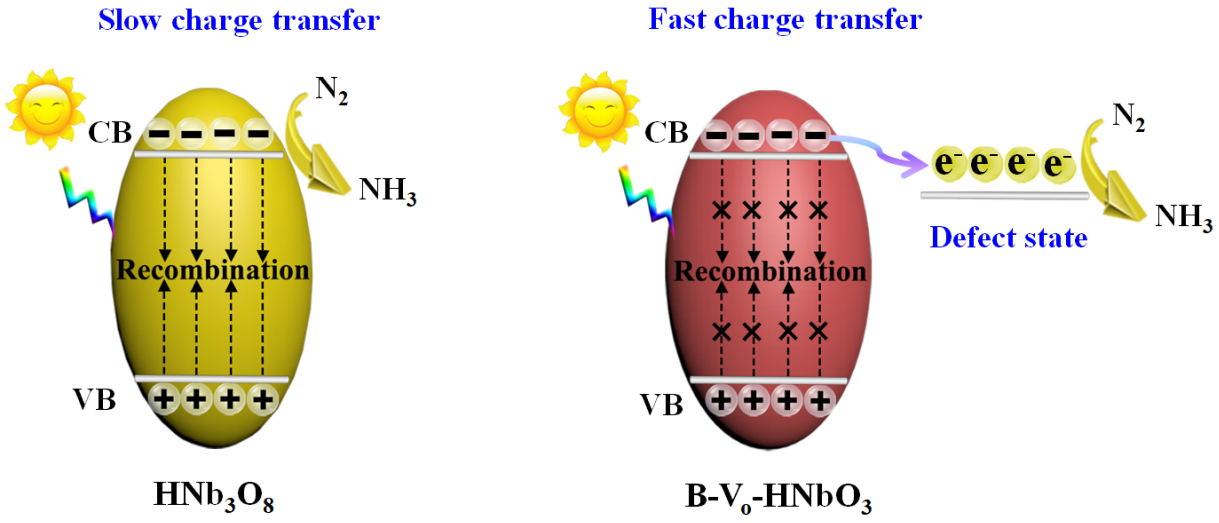

Figure S9. Illustrations of charge transfer and band structures of HNb_3O_8 and B-V_o-$HNbO_3$ NSs.

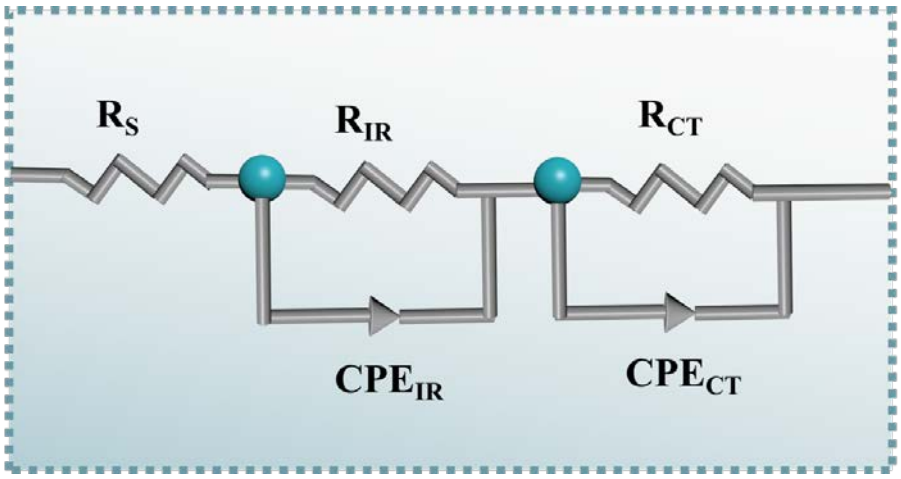

Figure S10. The equivalent circuit used for fitting the impedance data, where R_S represents the series resistance (including the material resistance and contact resistance of the test system), R_{IR} and CPE_{IR} at higher frequencies correspond to the bulk charge trapping resistance and constant phase element, respectively, and the R_{CT} and CPE_{CT} represent the interfacial charge transfer resistance and constant phase element, respectively.

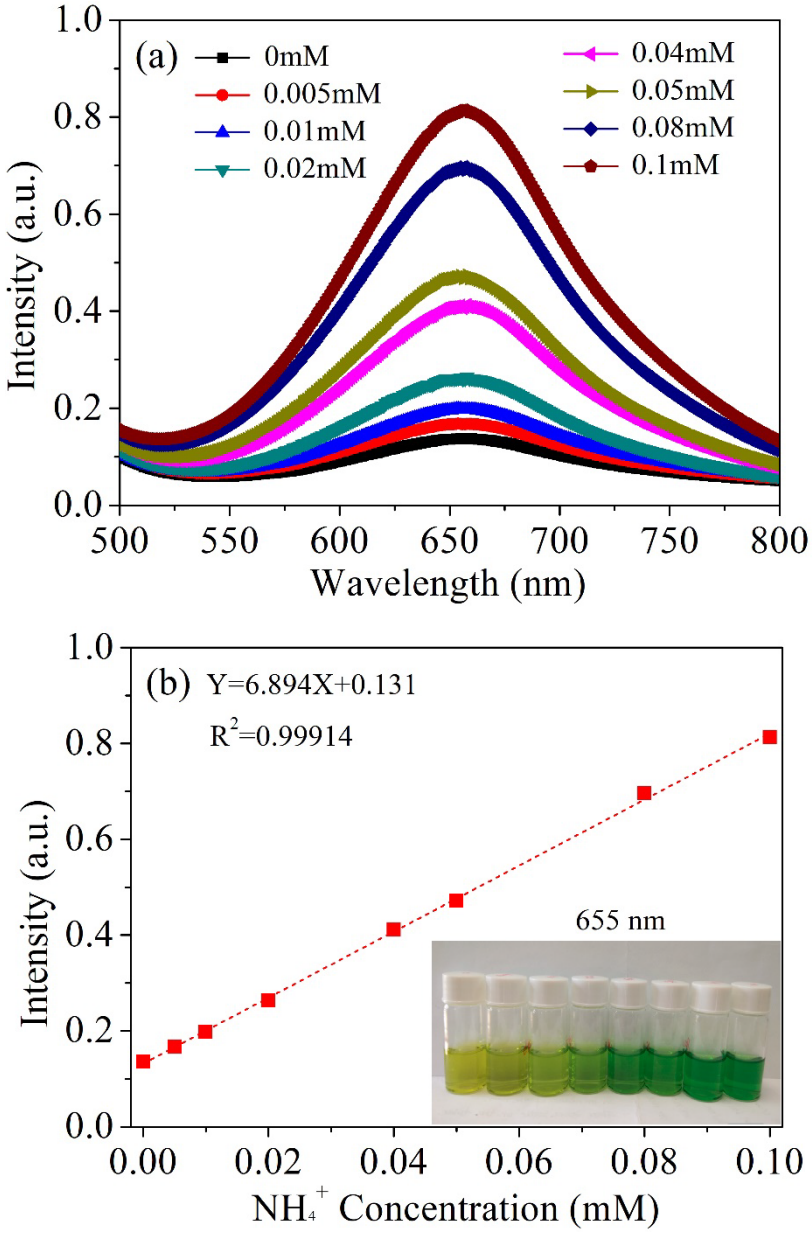

Figure S11. Determination of ammonia by the indophenol blue method. (a) UV-Vis absorption spectra of indophenol assays with NH_4Cl solution after incubated for 1 h at room temperature. (b) The corresponding calibration curve.

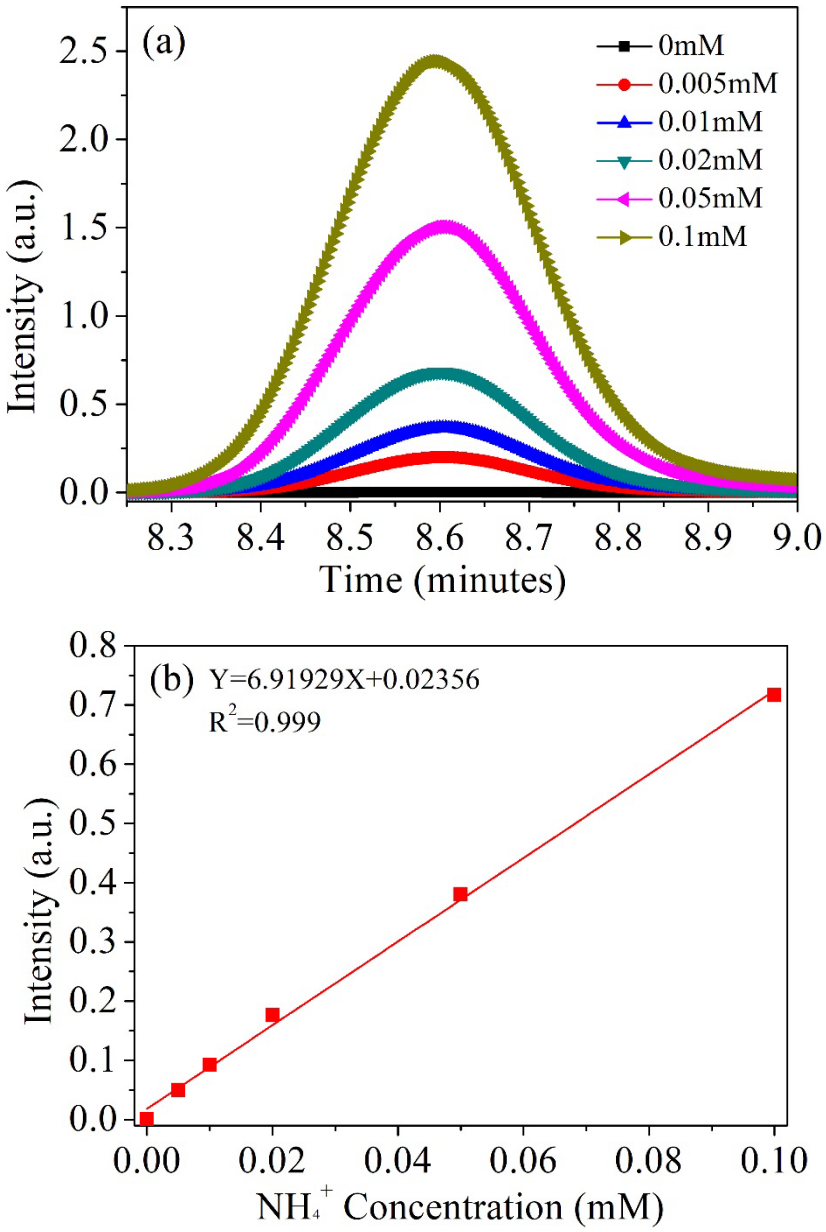

Figure S12. Determination of ammonia by the ion chromatograph method. (a) The ion chromatography data with a series of standard NH_4Cl solutions. (b) The corresponding calibration curve.

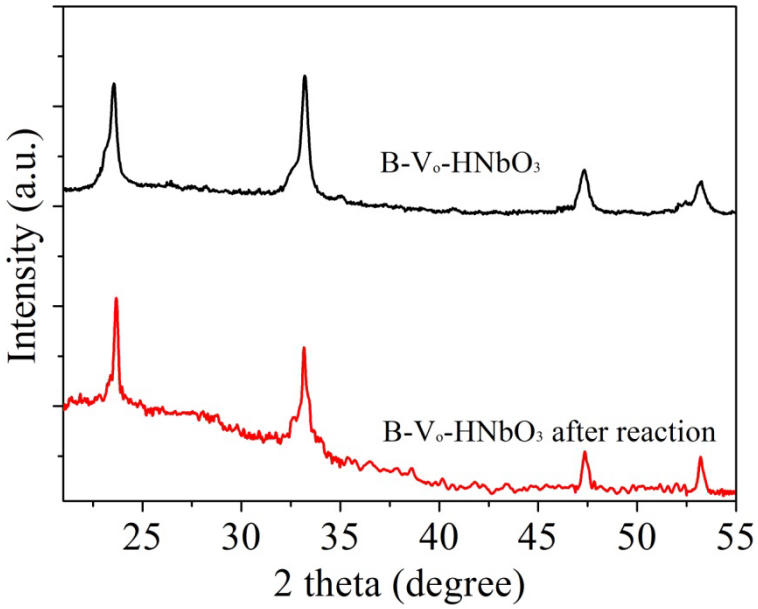

Figure S13. XRD patterns of B-V_o-$HNbO_3$ NSs as the photocatalysts before and after photocatalytic N_2 reduction reactions under light illumination.

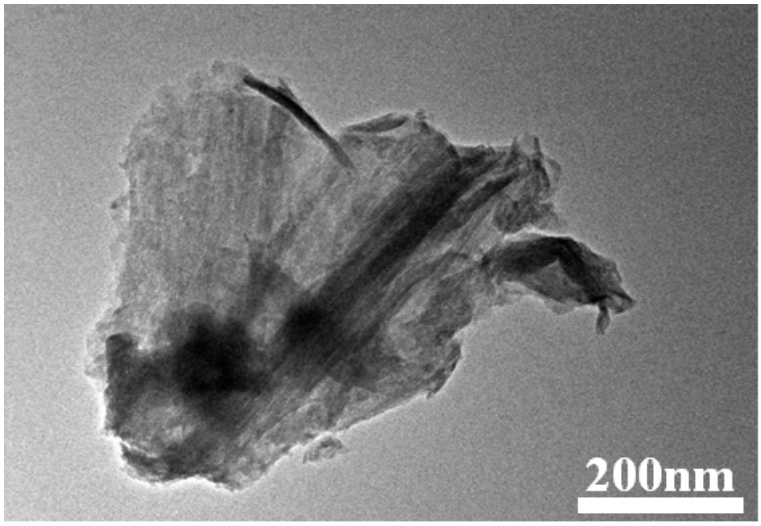

Figure S14. TEM image of B-V_o-$HNbO_3$ NSs as the photocatalysts after photocatalytic N_2 reduction reactions under light illumination.

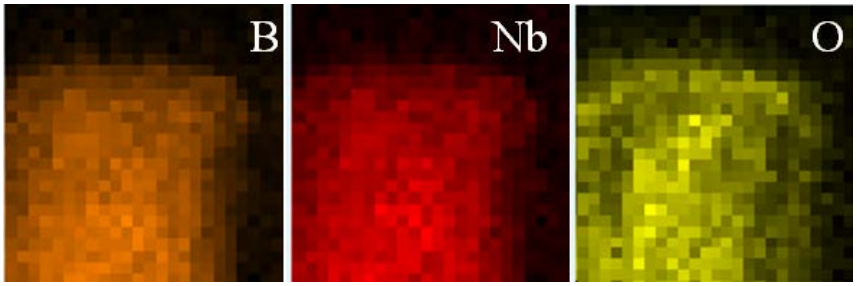

Figure S15. HAADF-STEM element mappings of B-V_o-$HNbO_3$ NSs as the photocatalysts after photocatalytic N_2 reduction reactions under light illumination.

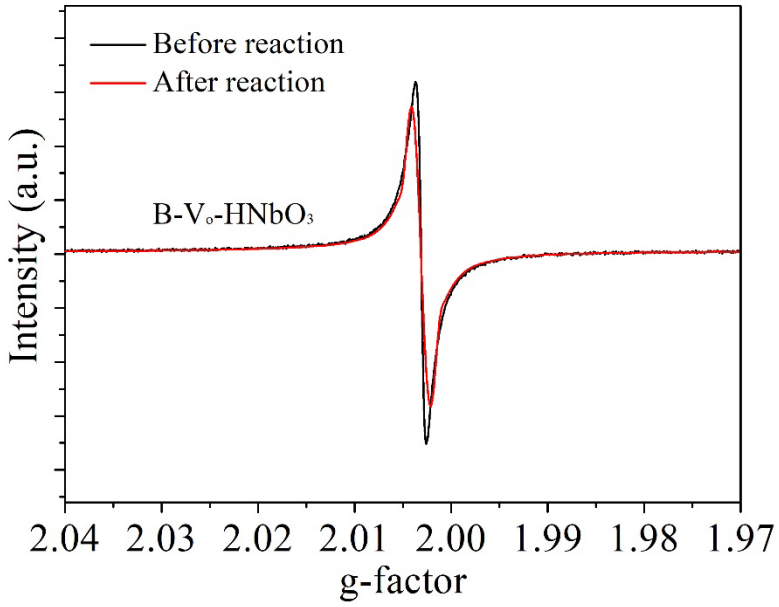

Figure S16. Electron paramagnetic resonance (EPR) spectra of B-V_o-$HNbO_3$ NSs as the photocatalysts before and after photocatalytic N_2 reduction reactions.

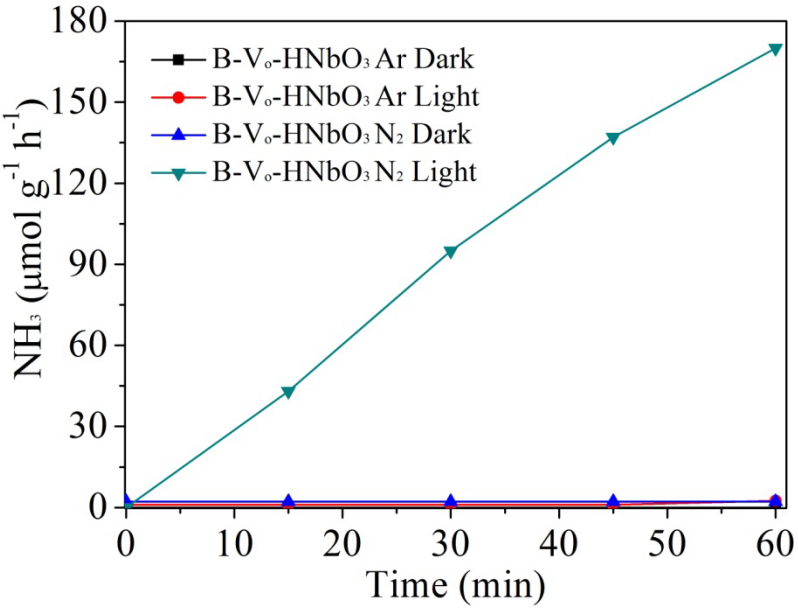

Figure S17. The photocatalytic NH_3 evolution tests were conducted by applying N_2 and Ar gas during the photocatalytic process under dark and light illumination conditions over B-V_o-$HNbO_3$ as photocatalyst.

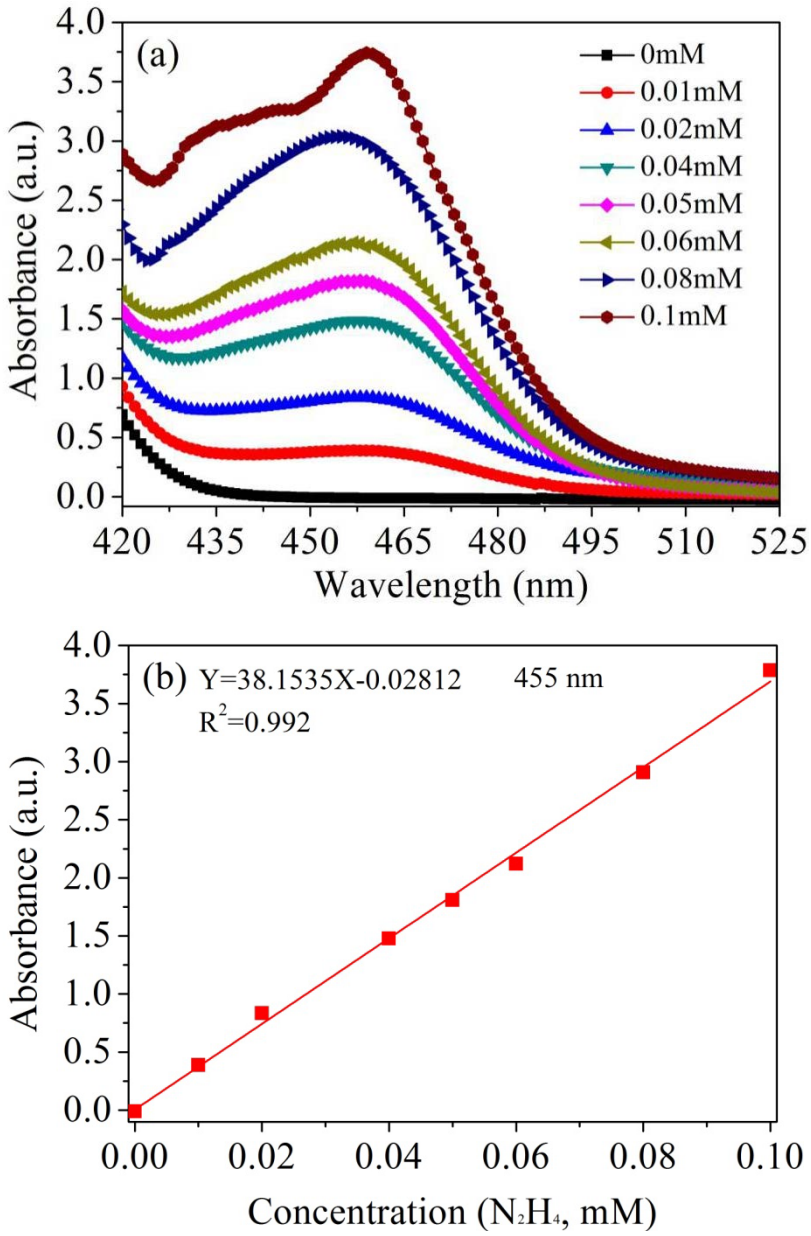

Figure S18. Determination of ammonia by the Watt and Chrisp method. (a) The UV-Vis absorption spectra of series hydrazine solutions after incubated for 30 min at room temperature. (b) The corresponding calibration curve.

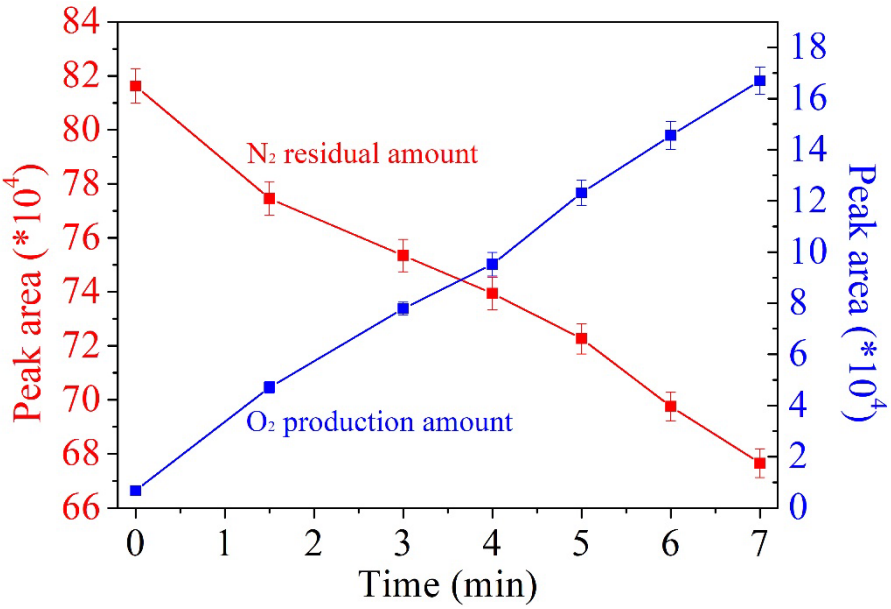

Figure S19. The photocatalytic O_2 evolution amount and residual N_2 amount using B-V_o-$HNbO_3$ NSs as catalyst during one cycle NRR reaction under solar illumination.

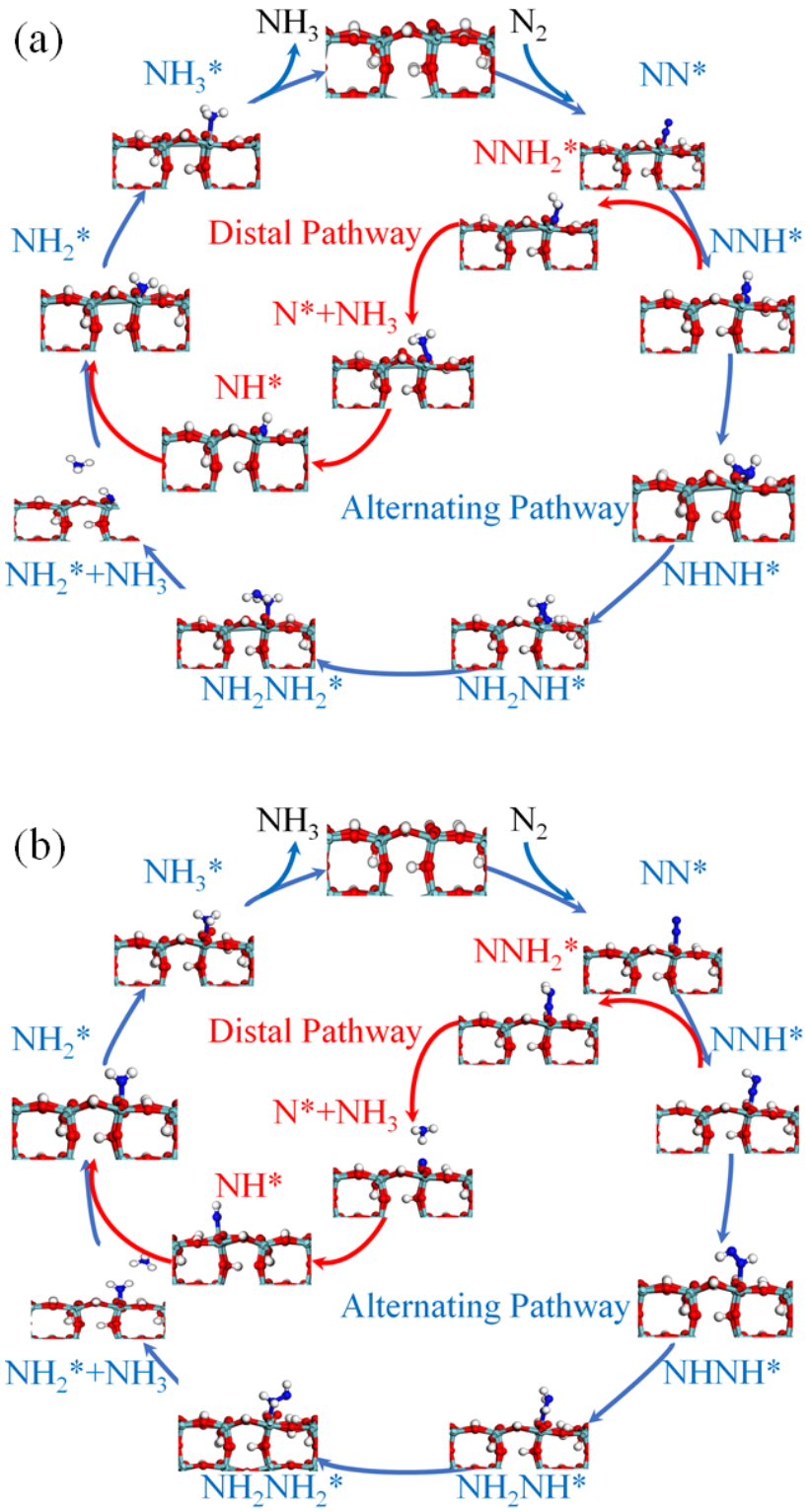

Figure S20. Optimized geometric structures of various intermediates (*NN, *NNH, *NHNH, *NH_2NH, *NH_2NH_2, *NH_2, and *NH_3) along the reaction path of the NRR that proceeded on (a) V_O-$HNbO_3$ and (b) B-$HNbO_3$.

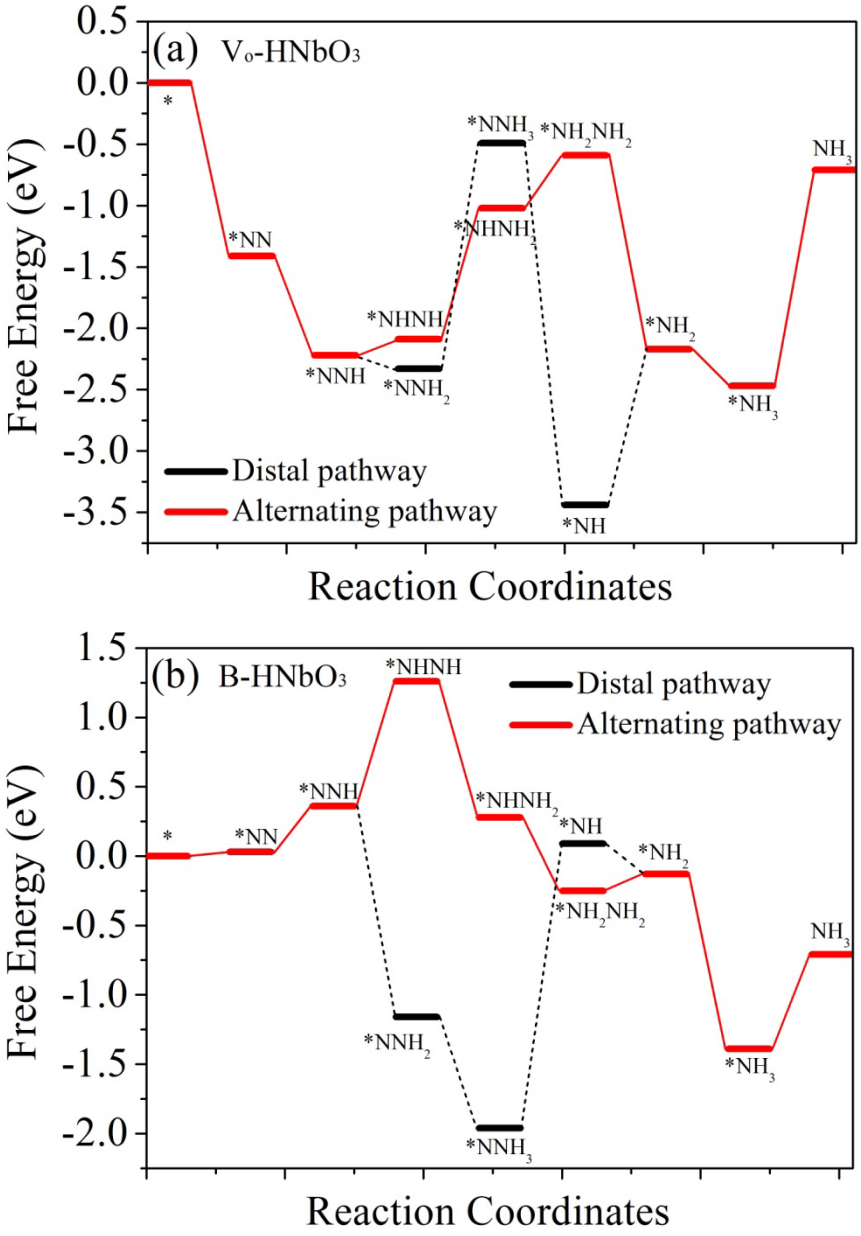

Figure S21. Free energy diagrams along the reaction path of the NRR that proceeded on (a) V_o-$HNbO_3$ and (b) B-$HNbO_3$.

Table S1. Summary of previous types of the photocatalysts for solar N_2 reduction to NH_3.

Photocatalyst	Light source	Scavenger	Test method	C(NH_3)	Ref.
Cu-doped ZnAl-LDH	UV-Vis	None	Nessler's reagent	110	[18]
6% Cu/TiO_2	UV-Vis	None	Nessler's reagent	78.9	[19]
MoO_{3-x} nanobelts	UV-vis	None	Indophenol blue	1.1	[20]
Mo/$W_{18}O_{49}$ nanowires	UV-vis	None	Indophenol blue	61.9	[21]
NiS/CdS nanorods	>420 nm	None	Indophenol blue	94.4	[22]
Sb/TiO_2 nanosheets	UV-vis	Methanol	Nessler's reagent	32.2	[23]
Au/TiO_2 nanosheets	>420 nm	Methanol	Nessler's reagent	130.5	[24]
Bi_2WO_6 nanodisks	UV-vis	None	Nessler's reagent	86	[25]
Ru/TiO_2 nanosheets	UV-vis	Ethanol	Nessler's reagent	3.31	[26]
Reduced TiO_2	>254 nm	2-propanol	Nessler's reagent	2.5	[27]
$AgInS_2$/MXene	>420 nm	Methanol	Nessler's reagent	38.8	[28]
Black Phosphorus /CdS	>420 nm	Methanol	Nessler's reagent	57.64	[29]
Defective ZnCr-LDH	UV-vis	None	Nessler's reagent	33.19	[30]
BiOBr nanosheets	>420 nm	None	Indophenol blue	104.2	[31]
BiOCl nanosheets	UV-vis	Methanol	Indophenol blue	92.4	[32]
Nb_2O_5/C/Nb_2C/g-C_3N_4	>420 nm	None	Nessler's reagent	31.5	[33]
B-V_o-$HNbO_3$ nanosheets	UV-vis	None	Nessler's reagent, IC	170	This work

References

1. Xiong, J.; Wen, L.; Jiang, F.; Liu, Y.; Liang, S.; Wu, L. Ultrathin HNb_3O_8 Nanosheet: An Efficient Photocatalyst for the Hydrogen Production. *J. Mater. Chem. A* **2015**, 3, 20627-20632.

2. Xu, W.; Gang, C.; Chao, Z.; Yu, Y.; Gang, W. N-Doped Nb_2O_5 Sensitized by Carbon Nitride Polymer-Synthesis and High Photocatalytic Activity under Visible Light. *Eur. J. Inorg. Chem.* **2012**, 11, 1742-1749.

3. Hirakawa, H.; Hashimoto, M.; Shiraishi, Y.; Takayuki, H. Photocatalytic Conversion of Nitrogen to Ammonia with Water on Surface Oxygen Vacancies of Titanium Dioxide. *J. Am. Chem. Soc.* **2017**, 139, 10929-10936.

4. Chen, X.; Zhang, X.; Li, Y.; Qi, M.; Li, J.; Tang, Z.; Zhou, Z.; Xu, Y. Transition Metal Doping BiOBr Nanosheets with Oxygen Vacancy and Exposed {102} Facets for Visible Light Nitrogen Fixation. *Appl. Catal. B* **2021**, 281, 119516.

5. Watt, G. W.; Chrisp, J. D. J. A. C. Spectrophotometric Method for Determination of Hydrazine. *Anal. Chem.* **1952**, 24, 2006-2008.

6. Li, H.; Gu, S.; Sun, Z.; Guo, F.; Xie, Y.; Tao, B.; He, X.; Zhang, W.; Chang, H. The In-Built Bionic "MoFe Cofactor" in Fe-Doped Two-Dimensional $MoTe_2$ Nanosheets for Boosting the Photocatalytic Nitrogen Reduction Performance. *J. Mater. Chem. A* **2020**, 8, 13038-13048.

7. Sakamoto, H.; Ohara, T.; Yasumoto, N.; Shiraishi, Y.; Hirai, T. Hot-Electron-Induced Highly Efficient O_2 Activation by Pt Nanoparticles Supported on Ta_2O_5 Driven by Visible Light. *J. Am. Chem. Soc.* **2015**, 137, 9324-9332.

8. Cui, D.; Wang, L.; Ren, K. Band-Gap Engineering of BiOCl with Oxygen Vacancies for Efficient Photooxidation Properties under Visible-Light Irradiation. *J. Mater. Chem. A* **2018**, 6, 2193-2199.

9. Seabold, J. A.; Choi, K. S. Efficient and Stable Photo-Oxidation of Water by a Bismuth Vanadate Photoanode Coupled with an Iron Oxyhydroxide Oxygen Evolution Catalyst. *J. Am. Chem. Soc.***2012**, 134, 2186-2192.

10. Kresse, G. G.; Furthmüller J. Efficient Iterative Schemes for *ab Initio* Total-Energy Calculations Using a Plane-Wave Basis Set. *Phys. Rev. B.* **1996**, 54, 11169-11186.

11. Perdew, J. P.; Burke, K.; Ernzerhof, M. Generalized Gradient Approximation Made Simple. *Phys. Rev. Lett.***1996**, 77, 3865-3868.

12. Kresse, G.; Joubert, D. From Ultrasoft Pseudopotentials to the Projector Augmented-Wave Method. *Phys. Rev. B.* **1999**, 59, 1758-1775.

13. Grimme, S.; Antony, J.; Ehrlich, S.; Krieg, H. A Consistent and Accurate *ab Initio* Parametrization of Density Functional Dispersion Correction (DFT-D) for the 94 Elements H-Pu. *J. Chem. Phys*. **2010**, 132, 154104.

14. Yang, G.; Hou, W.; Feng, X.; Jiang, X.; Guo, J. Density Functional Theoretical Studies on Polyaniline/HNb_3O_8 Layered Nanocomposites. *Adv. Funct. Mater.* **2010**, 17, 3521-3529.

15. Feng, Q. J. M. T. C. Electronic, Optical Properties and Stress-Driven Modulation of Monolayer MNb_3O_8 (M=H,Li,Na,K): An *ab-Initio* Investigation. *Mater. Today Commun.* **2020**, 101867.

16. Norskov, J. K.; Rossmeisl, J.; Logadottir, A.; Lindqvist, L.; Kitchin, J. R.; Bligaard, T.; Jonsson, H. Origin of the Overpotential for Oxygen Reduction at a Fuel-Cell Cathode. *J. Phys. Chem. B* **2004**, 108, 17886-17892.

17. Guo, X.; Gu, J.; Lin, S.; Zhang, S.; Chen, Z.; Huang, S. Tackling the Activity and Selectivity Challenges of Electrocatalysts toward the Nitrogen Reduction Reaction *via* Atomically Dispersed Biatom Catalysts. *J. Am. Chem. Soc*. **2020**, 142, 5709-5721.

18. Zhang, S.; Zhao, Y. X.; Shi, R.; Zhou, C.; Waterhouse, G. I. N.; Wu, L. Z.; Tung, C. H.; Zhang, T. R. Efficient Photocatalytic Nitrogen Fixation over $Cu^{\delta+}$-Modified Defective ZnAl-Layered Double Hydroxide Nanosheets. *Adv. Energy Mater.* **2020**, 10, 1901973.

19. Zhao, Y.; Zhao, Y.; Shi, R.; Wang, B.; Waterhouse, G. I. N.; Wu, L.; Tung, C.; Zhang, T. Tuning Oxygen Vacancies in Ultrathin TiO_2 Nanosheets to Boost Photocatalytic Nitrogen Fixation up to 700 nm. *Adv. Mater.* **2019**, 31, 1806482.

20. Li, Y.; Xin, C.; Zhang, M.; Zhu, Y.; Ren, W.; Mei, Z.; Meng, G.; Feng, P. Oxygen Vacancy-Rich MoO_{3-x} Nanobelts for Photocatalytic N_2 Reduction to NH_3 in Pure Water. *Catal. Sci. Technol.* **2019**, 9, 803-810.

21. Zhang, N.; Jalil, A.; Wu, D.; Chen, S.; Liu, Y.; Gao, C.; Ye, W.; Qi, Z.; Ju, H.; Wang, C.; Wu, X.; Song, L.; Zhu, J.; Xiong, Y. Refining Defect States in $W_{18}O_{49}$ by Mo Doping: A Strategy for Tuning N_2 Activation towards Solar-Driven Nitrogen Fixation. *J. Am. Chem. Soc*. **2018**, 140, 9434-9443.

22. Gao, X.; An, L.; Qu, D.; Jiang, W.; Chai, Y.; Sun, S.; Liu, X.; Sun, Z. Enhanced Photocatalytic N_2 Fixation by Promoting N_2 Adsorption with a Co-Catalyst. *Sci. Bull.* **2019**, 64, 918-925.

23. Zhao, Z.; Hong, S.; Yan, C.; Choi, C.; Jung, Y.; Liu, Y.; Liu, S.; Li, X.; Qiu, J.; Sun, Z. Efficient Visible-Light Driven N_2 Fixation over Two-Dimensional Sb/TiO_2 Composites. *Chem. Commun.* **2019**, 55, 7171-7174.

24. Yang, J.; Guo, Y.; Jiang, R.; Qin, F.; Zhang, H; Lu, W.; Wang, J. High-Efficiency "Working-in-Tandem" Nitrogen Photofixation Achieved by Assembling Plasmonic Gold Nanocrystals on Ultrathin Titania Nanosheets. *J. Am. Chem. Soc.* **2018**, 8497-8508.

25. Zhou, S.; Zhang, C.; Liu, J.; Liao, J.; Kong, Y.; Xu, Y.; Chen, G. Formation of an Oriented Bi_2WO_6 Photocatalyst Induced by *in Situ* Bi Reduction and Its Use for Efficient Nitrogen Fixation. *Catal. Sci. Technol.* **2019**, 9, 5562-5566.

26. Liu, S.; Wang, Y.; Wang, S.; You, M.; Zhao, Z.; Jiang, G.; Qiu, J.; Wang, B.; Sun, Z. Photocatalytic Fixation of Nitrogen to Ammonia by Single Ru Atom Decorated TiO_2 Nanosheets. *ACS Sustain. Chem. Eng.* **2019**, 7, 6813-6820.

27. Hirakawa, H.; Hashimoto, M.; Shiraishi, Y.; Hirai, T. Photocatalytic Conversion of Nitrogen to Ammonia with Water on Surface Oxygen Vacancies of Titanium Dioxide. *J. Am. Chem. Soc.* **2017**, 139, 10929-10936.

28. Qin, J.; Hu, X.; Li, X.; Yin, Z.; Liu, B.; Lam, K. H. J. N. E. 0D/2D $AgInS_2$/MXene Z-Scheme Heterojunction Nanosheets for Improved Ammonia Photosynthesis of N_2. *Nano Energy* **2019**, 61, 27-35.

29. Shen, Z. K.; Yuan, Y. J.; Wang, P.; Bai, W.; Zou, Z. Few-Layer Black Phosphorus Nanosheets: A Metal-Free Cocatalyst for Photocatalytic Nitrogen Fixation. *ACS Appl. Mater. Interfaces* **2020**, 12, 17343-17352.

30. Zhao, Y. X.; Zheng, L. R.; Shi, R.; Zhang, S.; Bian, X. N.; Wu, F.; Cao, X. Z.; Waterhouse, G. I. N.; Zhang, T. Alkali Etching of Layered Double Hydroxide Nanosheets for Enhanced Photocatalytic N_2 Reduction to NH_3. *Adv. Energy Mater.* **2020**, 10, 2002199.

31. Li, H.; Shang, J.; Ai, Z.; Zhang, L. Efficient Visible Light Nitrogen Fixation with BiOBr Nanosheets of Oxygen Vacancies on the Exposed {001} Facets. *J. Am. Chem. Soc.* **2015**, 137, 6393-6399.

32. Li, H.; Shang, J.; Shi, J. G.; Zhao, K.; Zhang, L. Facet-Dependent Solar Ammonia Synthesis of BiOCl Nanosheets *via* a Proton-Assisted Electron Transfer Pathway. *Nanoscale* **2016**, 8, 1986-1993.

33. Jiang, H.; Zang, C.; Zhang, Y.; Wang, W.; Yang, C.; Sun, B.; Shen, Y.; Bian, F. 2D MXene-Derived Nb_2O_5/C/Nb_2C/g-C_3N_4 Heterojunctions for Efficient Nitrogen Photofixation. *Catal. Sci. Technol.* **2020**, 10, 5964-5972.